Accepted Manuscript

Early tumor detection afforded by *in vivo* imaging of near-infrared II fluorescence

Zhimin Tao, Xiangnan Dang, Xing Huang, Mandar D. Muzumdar, Eric S. Xu, Neelkanth Manoj Bardhan, Haiqin Song, Ruogu Qi, Yingjie Yu, Ting Li, Wei Wei, Jeffrey Wyckoff, Michael J. Birrer, Angela M. Belcher, Ph.D, Charles W. and Jennifer C. Johnson Clinical Investigator, P. Peter Ghoroghchian, M.D., Ph.D, W.M. Keck Professor of Energy

PII: S0142-9612(17)30283-1

DOI: 10.1016/j.biomaterials.2017.04.046

Reference: JBMT 18066

To appear in: *Biomaterials*

Received Date: 22 November 2016

Revised Date: 24 April 2017

Accepted Date: 24 April 2017

Please cite this article as: Tao Z, Dang X, Huang X, Muzumdar MD, Xu ES, Bardhan NM, Song H, Qi R, Yu Y, Li T, Wei W, Wyckoff J, Birrer MJ, Belcher AM, Ghoroghchian PP, Early tumor detection afforded by *in vivo* imaging of near-infrared II fluorescence, *Biomaterials* (2017), doi: 10.1016/j.biomaterials.2017.04.046.

DOI: 10.1002/ ((please add manuscript number))
Article type: Original Research

Title: Early Tumor Detection Afforded by *In Vivo* Imaging of Near-Infrared II Fluorescence

Zhimin Tao,[1,+] Xiangnan Dang,[1,+] Xing Huang,[1] Mandar D. Muzumdar,[1,2] Eric S. Xu,[1] Neelkanth Manoj Bardhan,[1] Haiqin Song,[1] Ruogu Qi,[1] Yingjie Yu,[1] Ting Li,[1,3] Wei Wei,[3] Jeffrey Wyckoff,[1] Michael J. Birrer,[3] Angela M. Belcher,[1,*] and P. Peter Ghoroghchian[1,2,*]

[1] Koch Institute for Integrative Cancer Research, Massachusetts Institute of Technology, 77 Massachusetts Avenue, Building 76, Cambridge, MA 02139, United States
[2] Dana-Farber Cancer Institute, 450 Brookline Avenue, Boston, MA 02115, United States
[3] Department of Medicine, Massachusetts General Hospital, 55 Fruit Street, Boston, MA 02114, United States

+ These authors contributed equally

* To whom correspondence should be addressed:

Angela M. Belcher, Ph.D.
W.M. Keck Professor of Energy
Department of Material Science and Engineering and Department of Biological Engineering
Koch Institute for Integrative Cancer Research
Massachusetts Institute of Technology
77 Massachusetts Avenue, 76-561A
Cambridge, MA 02139, USA
(617) 252-1163
belcher@mit.edu

P. Peter Ghoroghchian, M.D., Ph.D.
Charles W. and Jennifer C. Johnson Clinical Investigator
Koch Institute for Integrative Cancer Research
Massachusetts Institute of Technology
77 Massachusetts Avenue, 76-261F
Cambridge, MA 02139, USA
(617) 252-1163
ppg@mit.edu

KEYWORDS: Lanthanide nanoparticles, optical imaging, ovarian cancer, tumor targeting

ABSTRACT

Cell-intrinsic reporters such as luciferase (LUC) and red fluorescent protein (RFP) have been commonly utilized in preclinical studies to image tumor growth and to monitor therapeutic responses. While extrinsic reporters that emit near infrared I (NIR-I: 650 - 950 nm) or near-infrared II (NIR-II: 1000 - 1700 nm) optical signals have enabled minimization of tissue autofluorescence and light scattering, it has remained unclear as to whether their use has afforded more accurate tumor imaging in small animals. Here, we developed a novel optical imaging construct comprised of rare earth lanthanide nanoparticles coated with biodegradable diblock copolymers and doped with organic fluorophores, generating NIR-I and NIR-II emissive bands upon optical excitation. Simultaneous injection of multiple spectrally-unique nanoparticles into mice bearing tumor implants established via intraperitoneal dissemination of LUC^+/RFP^+ OVCAR-8 ovarian cancer cells enabled direct comparisons of imaging with extrinsic vs. intrinsic reporters, NIR-II vs. NIR-I signals, as well as targeted vs. untargeted exogenous contrast agents in the same animal and over time. We discovered that *in vivo* optical imaging at NIR-II wavelengths facilitates more accurate detection of smaller and earlier tumor deposits, offering enhanced sensitivity, improved spatial contrast, and increased depths of tissue penetration as compared to imaging with visible or NIR-I fluorescent agents. Our work further highlights the hitherto underappreciated enhancements in tumor accumulation that may be achieved with intraperitoneal as opposed to intravenous administration of nanoparticles. Lastly, we found discrepancies in the fidelity of tumor uptake that could be obtained by utilizing small molecules for *in vivo* as opposed to *in vitro* targeting of nanoparticles to disseminated tumors.

INTRODUCTION

Fluorescent contrast agents have been widely used in biomedical research and hold promise for translational applications [1, 2]. Fluorophores that emit visible light (350-650 nm) have been shown to generate highly sensitive signals that have enabled (sub-) cellular imaging via *in vitro* and *in vivo* (i.e. intravital) microscopy [2]. Those that emit light in the near infrared I spectrum (NIR-I: 650-950 nm) have exhibited increased depths of tissue penetration and have been utilized in whole animal or clinical imaging applications [3]. Recently, it has also been demonstrated that optical imaging in the short-wave infrared or the near-infrared II spectrum (NIR-II: 1000-1700 nm) provides additional advantages due to further minimizations in tissue autofluorescence and light scattering [4, 5]. As a result, NIR-II emissive agents have been developed to afford maximal depths of signal penetration and enhanced contrast resolution for *in vivo* optical imaging [6, 7].

Unfortunately, only a handful of agents have been reported to fluorescence in the NIR-II spectral window, including a few organic fluorophores [8-10], carbon nanotubes [4, 6, 11-20], quantum dots [21-25], and lanthanide nanoparticles (LNPs) [26-32]. Among them, the organic fluorophores have exhibited very low NIR-II fluorescence quantum yields while quantum dots and LNPs have displayed the highest [33, 34]. For small animal imaging applications, LNPs offer many advantages, including tunable multiplex emission upon excitation at a single wavelength (through substitutions of lanthanide dopants), superior chemical and photostability, improved biocompatibility, as well as facile surface functionalization [35-40]. There have been many examples of utilizing up-conversion (UC) fluorescence from LNPs in preclinical imaging studies [41-49]. Recently, LNPs have also been shown to generate NIR-II signals following X-ray [26] or 980 nm laser excitation [27], enabling sensitive and high-resolution *in vivo* optical imaging.

To date, however, there have been no studies that have sought to rigorously compare the fidelity of tumor imaging that could be afforded by detecting NIR-II vs. NIR-I emissive signals, whether generated from an organic fluorophore or from any inorganic-based agent. The utility of using a targeted vs. untargeted exogenous fluorophore, especially in comparison to intrinsic reporters such as luciferase (LUC) and red fluorescent protein (RFP), have not been conclusively established in preclinical animal models. Further, there have been no reports of simultaneous *in vivo* imaging of different reporters in a single animal that contained a multitude of tumors at varying depths. While *in vivo* imaging of LUC and/or RFP has been extensively used to follow tumor growth and to determine therapeutic responses to experimental agents, these intrinsic reporters have correlated poorly with tumor measurements made by CT or MRI in the same animals [2]. It has also remained unclear as to whether a NIR-II or NIR-I emissive agent could promote more accurate *in vivo* imaging for such preclinical applications, which could help to supplant the use of intrinsic reporters.

To address these challenges, we utilized LNPs comprised of sodium yttrium fluoride ($NaYF_4$) doped with ytterbium (Yb) and either erbium (Er) or holmium (Ho) with or without thulium (Tm). Yb served as an acceptor ion that absorbed excitation light at 980 nm while Er, Tm, and Ho then generated various visible and NIR-I emission bands (through UC energy transfer) as well as signals in the NIR-II spectrum. To generate water-soluble contrast agents for *in vivo* imaging, we further coated these LNPs with a diblock copolymer of poly(ethylene oxide)-block-poly(ε-caprolactone) (PEO-b-PCL), generating core-shell nanoparticles with fully PEGylated surfaces. Comprised of two-FDA approved building blocks [50], PEO-b-PCL has been previously shown to form nanoparticles that are biodegradable, that exhibit prolonged circulatory half-lives, and that evade *in vivo* immune recognition and uptake [51]. PCL is known to slowly degrade through hydrolysis of ester linkages, leading to safe byproducts that do not affect local pH nor induce otherwise deleterious environmental reactions [52]. The

lipophilic carbocyanine dye 1,1'-dioctadecyl-3,3,3',3'-tetramethylindotricarbocyanine iodide (DiR) was further incorporated within the PCL shell of our nanoparticles; DiR has previously been shown to enable accurate tumor imaging of PEO-b-PCL micelles in subcutaneous tumor xenograft models [53, 54]. Utilization of DiR in our studies enabled direct comparisons between imaging of NIR-I emission from this conventional organic fluorophore (in the nanoparticle shell) to detection of NIR-I UC and NIR-II emissive bands generated from the inorganic LNPs (in the nanoparticle core).

To directly compare various imaging parameters afforded by detection of our core-shell nanoparticles with those obtained by employing cell intrinsic reporters, we utilized an *in vivo* animal model comprised of nude mice that were xenotransplanted with LUC^+/RFP^+ OVCAR-8 human ovarian cancer cells via peritoneal dissemination. OVCAR-8 has been shown to be a high-grade serous ovarian cancer cell line; and, intraperitoneal (IP) injection of OVCAR-8 cells has previously been used to establish a murine model of advanced human ovarian cancer for basic investigation and preclinical development [55, 56]. Imaging was conducted at various time points after tumor cell implantation to compare the imaging sensitivity and resolution afforded by utilizing each agent (i.e. intrinsic LUC and RFP signals as well as NIR-I, NIR-I UC and NIR-II emission from the core-shell nanoparticles) to detect tumor implants within the peritoneum of the animals. Additionally, the folate receptor (FR) is known to be highly expressed in > 90% of human ovarian cancer cells [57, 58]; and, folic-acid (FA) has previously been conjugated to exogenous contrast agents to enable targeting of ovarian cancers in both preclinical and clinical studies [59]. To examine the utility of FR targeting to enhance the *in vivo* tumor accumulation of our nanoparticles, two sets of constructs were generated comprised of untargeted (PEO-b-PCL-wrapped $NaYF_4$:Yb,Er-based LNPs) and FR-targeted core-shell nanoparticles (FA-conjugated PEO-b-PCL-wrapped $NaYF_4$:Yb,Ho-based LNPs). Imaging commenced after either IP or intravenous (IV) injection of both sets of

nanoparticles in order to compare the relative tumor accumulation obtained via each of these routes of administration. Both IP and IV delivery of chemotherapeutics are currently utilized in the treatment of locally advanced ovarian cancers; but, there are conflicting clinical data as to their relative efficacy [59]. Simultaneous injection of spectrally unique nanoparticles into mice bearing disseminated LUC^+/RFP^+ OVCAR-8 ovarian tumors enabled direct comparisons of imaging with extrinsic vs. intrinsic reporters, with various NIR-II vs. NIR-I signals, as well as with FR-targeted vs. untargeted exogenous contrast agents in the same animal, at differing tissue depths, and longitudinally over time.

MATERIALS AND METHODS

Full descriptions of nanoparticle preparations, materials and optical characterizations, as well as all *in vitro*, *in vivo* and *ex vivo* experiments with different formulations may be found in the *Supplemental Materials and Methods* in the accompanying Supporting Information.

***In Vivo* and *Ex Vivo* Imaging of Core-Shell Nanoparticles**. *In vivo* and *ex vivo* imaging of cell intrinsic reporters (LUC and RFP), as well as imaging of DiR (NIR-I) emission from core-shell nanoparticles in whole mice, their excised organs, and in blood (microcapillary tubes), were conducted using an IVIS Spectrum bioluminescent and fluorescent imaging system (PerkinElmer; Akron, Ohio; note that for imaging of DiR, λ_{ex} = 710 nm; λ_{em} = 800 nm). NIR-I UC and NIR-II emission from the same core-shell nanoparticles were concurrently imaged using a custom designed instrument [6, 7, 17], which was equipped with 808 nm and 980 nm lasers diodes (CNI Laser; China), a silicon camera for bright-field images (Hamamatsu, ORCA-Flash4.0 LT; Japan), and a liquid nitrogen-cooled InGaAs camera for NIR-II fluorescence imaging (256 × 320 pixel array, detection range: 800 - 1700 nm; Princeton Instruments, OMA:V 2D; Acton, MA). In front of the InGaAs detector, a NIR camera lens was attached (SWIR-2, Navitar; Rochester, NY). Two long-pass emission filters

with a cut-off wavelength of 1400 nm (Thorlabs; Newton, NJ) and two band-pass filters (1575 ± 25 nm; Thorlabs) were also employed. In front of the silicon detector, a second camera lens was attached (MVL25M1, Navitar). Two short-pass filters with a cut-off wavelength of 900 nm (Thorlabs) and two notch filters (980 ± 40 nm; Edmund Optics, Barrington, NJ) were also utilized.

For excitation of LNPs, an optical fiber coupled to the 980 nm laser diode (CNI Laser) was used and a laser line filter centered at 980 nm (Edmund Optics) was mounted in front of the laser to remove any unwanted excitation light. The actual fluence (energy density) of the mouse during *in vivo* imaging was ~100 mW/cm^2 and the acquisition time was 0.1 ~ 1 s. For the contrast images, white light illumination was utilized. Custom designed software (generated using Visual Basic and LabView; National Instruments, Austin, TX) was used to control the lasers and the cameras during imaging. Protective eyewear was utilized during image acquisition. Co-registration of bright-field and fluorescence images, as well as subsequent image processing, were performed using custom-designed algorithms (Matlab; MathWorks, Natick, MA). Quantification of fluorescence intensities for biodistribution and pharmacokinetic analyses were conducted using ImageJ software (NIH).

Study Approval: All animal handling and procedures were conducted in compliance with the rules and regulations set forth by the Committe on Animal Care at MIT. Animals were housed and maintained in the vivarium on the 7th Floor of the Koch Institute building (76) at MIT, following guidelines established by MIT's Division of Comparative Medicine (DCM) under a pre-approved protocol (0113-007-16).

RESULTS

Synthesis and Characterization of Core-Shell Nanoparticles. Oleic acid-coated LNPs comprised of $NaYF_4$, and which were doped with Yb and either Er or Ho with and without Tm, were prepared following established protocols with minor modifications [60, 61]. The formation of core-shell nanoparticles comprised of polymer-wrapped LNPs occurred immediately after aqueous dispersion of a THF solution of oleic acid-coated LNPs, DiR, and PEO-b-PCL diblock copolymer (**Scheme S1**). The relative hydrophobic nature of DiR and the LNPs drove their segregation into the hydrophobic PCL compartment of the assembled nanoparticles. The hydrophilic PEO corona enabled aqueous dissolution of the nanocomposite and stabilized its core-shell structure. Optimization of the sonication power and the initial mass ratio of polymer-to-LNP established a reproducible protocol for generating core-shell nanoparticles (see *Supplemental Materials and Methods* and **Figure S1**). Core-shell nanoparticles were further engineered to incorporate the organic NIR-I fluorophore DiR within their PCL shells (**Figure S2**). Three imaging constructs were preferentially utilized in this study: two untargeted core-shell nanoparticles (DiR-Er,Tm/PEO-PCL and DiR-Er/PEO-PCL) as well as an FR-targeted formulation (DiR-Ho/Folate-PEO-PCL), representing DiR-encapsulated PEO_{5k}-PCL_{16k}-coated $NaYF_4$:Yb,Er,Tm-, PEO_{5k}-PCL_{16k}-coated $NaYF_4$:Yb,Er-, and FA-conjugated PEO_{6k}-PCL_{16k}-coated $NaYF_4$:Yb,Ho-based LNPs, respectively.

Figure 1A illustrates the structure of the core-shell nanoparticle, wherein the PEO-b-PCL shell is depicted as a yellow micelle, the LNPs as blue cubes, and the organic fluorophore DiR as red dots. The structures of the actual nanocomposites were verified by cryo-TEM and the core-shell nanoparticles were found to be approximately 60-90 nm in diameter (**Figure 1B**); note that the core LNPs were each ~20 nm in size. Each core-shell nanoparticle formulation (DiR-Er,Tm/PEO-PCL, DiR-Er/PEO-PCL, and DiR-Ho/Folate-PEO-PCL) was further characterized by dynamic light scattering (DLS) in order to measure its average

hydrodynamic diameter and its polydispersity index (PDI) in suspension; its average surface charge was also determined through zeta potential measurements (**Figures S3-S5**).

These physicochemical properties as well as the synthetic yields and compositions of all components in each formulation are summarized in **Table S1**. For each core-shell nanoparticle formulation, the optical properties of each of its emissive components were independently measured in order to verify their presence in the final aqueous suspensions (e.g. **Figure S3E**). When excited at 700 nm, an emissive signal that peaked at 778 nm was generated that corresponded to the NIR-I emission of DiR; exciting the same formulation at 980 nm, however, resulted in simultaneous UC (visible and NIR-I) and NIR-II emission from DiR-Er,Tm/PEO-PCL (**Figure S3E**), DiR-Er/PEO-PCL (**Figure S4E**), and DiR-Ho/Folate-PEO-PCL (**Figure S5E**). Additional processing steps enabled the isolation of homogeneous populations of core-shell nanoparticles from suspensions that included PEO-b-PCL (shell) nanoparticles (see *Supplemental Materials and Methods* and **Figure S6**); but, these steps were not deemed essential as all core-shell nanoparticle formulations demonstrated analogous material (size, charge, concentration) and optical properties (absorbance and fluorescence intensities), enabling accurate imaging comparisons between different formulations.

980 nm excitation of core LNPs generated fluorescence bands in the visible range, consistent with a well-known process of UC energy transfer [62], as well as simultaneous NIR-II fluorescence with a peak at 1566 nm and 1162 nm for Er- and Ho- based LNPs, respectively. For core-shell nanoparticles that contained $NaYF_4$:Yb,Er,Tm-based LNPs, the presence of Tm^{3+} generated another major NIR-I UC peak at 800 nm; other peaks from this composition were similar to those of core-shell nanoparticles that incorporated $NaYF_4$:Yb,Er-based LNPs. The intensities of the LNPs' UC emission processes scaled with $(\text{power})^2$ while that of their NIR-II fluorescence increased linearly with laser power (**Figure S7**); similar power-

dependent emission phenomena have previously aided in the *in vivo* detection of NIR-I UC signals from LNP formulations [63].

In addition to the emission of these extrinsic reporters, bioluminescence due to the luciferase-luciferin reaction and RFP fluorescence upon 535 nm excitation are also included in **Figure 1C**, generating a spectral comparison of all reporters that were subsequently utilized for *in vivo* and *ex vivo* imaging (*vide infra*). Prior to embarking on comparisons of *in vivo* imaging with different reporters, we examined the photostability of each of the emissive components within the core-shell nanoparticles. Nanoparticle suspensions were exposed to continuous laser irradiation for 1 h; NIR-I UC or NIR-II fluorescence from LNPs that were either suspended in organic solvent or incorporated in aqueous suspensions of core-shell nanoparticles were found to retain > 98% of their initial intensities at the end of the study (**Figure 1D**). Compared to free DiR in THF, whose fluorescence decreased by over 30% after 1 h of continuous excitation, DiR that was incorporated within the PCL shell of the nanoparticles maintained 88% of its initial emission intensity under the same conditions, exhibiting improved photo-resistance in the polymeric environment.

Imaging Fidelity and Sensitivity of Visible, NIR-I, and NIR-II Optical Reporters. We next compared the accuracy of *in vivo* imaging afforded by detection of cell intrinsic reporters (LUC and RFP) as compared to NIR-I vs. NIR-II emissive signals generated from our core-shell nanoparticles. LUC^+/RFP^+ OVCAR-8 cells were implanted into nude mice via IP injection, establishing a disseminated cell-line xenograft model of ovarian cancer. Peritoneal tumor implants were allowed to develop over a period of two weeks (4 mice); imaging then commenced at 72 h after IP injection of untargeted core-shell nanoparticles (DiR-Er,Tm/PEO-PCL) (**Figure 2A**); note that this time delay between nanoparticle injection and imaging allowed for systemic diffusion and *in vivo* tumor accumulation. Each mouse was imaged

using different luminescence and fluorescence detection systems. Optical imaging of intrinsic LUC and RFP signals ($\lambda_{ex}/\lambda_{em}$ = 535/600 nm), as well as NIR-I emission from DiR ($\lambda_{ex}/\lambda_{em}$ = 710/800), was conducted using an IVIS imaging system equipped with white light excitation and appropriate filters for fluorescence detection; luciferase bioimaging commenced 10 min after IP injection of luciferin and did not utilize excitation or emission filters. Imaging of NIR-I UC ($\lambda_{ex}/\lambda_{em}$ = 980/800 nm) and NIR-II fluorescence ($\lambda_{ex}/\lambda_{em}$ = 980/1175 nm or 980/1575 nm) was conducted using a custom-designed imaging instrument [6, 7, 17].

From the *in vivo* images (**Figure 2A,** *top row*), it was clear that the LUC and RFP signals co-localized with one another; imaging of RFP fluorescence, however, offered better visualization of individual tumor deposits and detected additional implants that were not visualized by bioluminescence imaging. Imaging of NIR-I signals from DiR demonstrated a poor association between nanoparticle (NIR-I) and tumor (RFP) biodistribution while imaging of UC-emission (NIR-I UC) from core LNPs correlated with the detection of intrinsic reporters for a tumor deposit in the left upper quadrant of each animal. Imaging of NIR-II fluorescence from core LNPs (NIR-II) demonstrated numerous tumor deposits, many of which corresponded with the same tumor sites that were detected by LUC and RFP imaging; but, it did also highlight other potential implants that were not otherwise visualized.

Upon completion of *in vivo* imaging, mice were sacrificed and their major organs were extracted in order to compare *in vivo* and *ex vivo* images of tumor locations and numbers as well as those of the nanoparticles and their relative biodistribution. *Ex vivo* imaging of RFP signals in whole organs demonstrated tumor implants on the serosal surfaces of the ovaries (bilaterally), pancreas, duodenum, liver, spleen, stomach, and intestines (**Figure 2A,** *bottom row*), which matched the known patterns of peritoneal dissemination for human epithelial ovarian cancers [64]; note that the *ex vivo* correlation between RFP and LUC signals was

poor, which was attributed to the short half-life of the luciferin/luciferase reaction and the time between *in vivo* substrate injection, animal sacrifice, and *ex vivo* imaging. As such, the relative RFP signal intensity in each excised organ was used as a baseline to compare the fidelity of *in vivo* and *ex vivo* imaging results that were obtained with other fluorescent channels. *Ex vivo* imaging of NIR-I signals from DiR, again, correlated poorly to most areas with RFP fluorescence; detection of DiR emission did, however, correctly identify two tumor deposits on the duodenum and pancreas that were seen with RFP imaging. In contrast, *ex vivo* imaging of NIR-I UC emission of core LNPs provided a better correlation with the biodistribution of RFP signals; NIR-II emission from the same particles, however, showed a nearly identical pattern of distribution to that of RFP.

Confocal microscopy of excised tumor sections confirmed co-localization of RFP (tumor) and UC emission (nanoparticle), demonstrating that the nanoparticles accumulated both in the perivascular spaces of large tumor deposits as well as in a punctate distribution pattern that was consistent with uptake into individual infiltrating tumor cells (**Figures 2B** and **S8**); note that there was an absence of nanoparticle uptake in normal healthy tissues, including those of the reticulo-endothelial system (i.e. the liver and spleen), after this IP route of administration. When comparing these *ex vivo* imaging results with those obtained by *in vivo* imaging of RFP, it was evident that increased contrast sensitivity and the identification of greater numbers of individual tumor deposits were afforded by *in vivo* imaging of core-shell nanoparticles at NIR-II wavelengths (**Figures 3A** and **S9A**). Further, there were superior correlations between the relative *in vivo* and *ex vivo* signal intensities, as well as the tissue distribution patterns of tumor deposits, obtained by detection of NIR-II emissive signals as compared to imaging with all other optical reporters.

To compare the utility of each intrinsic and extrinsic reporter for early tumor detection, we next conducted *in vivo* imaging studies of mice at 1-week post-IP implantation of LUC^+/RFP^+ OVCAR-8 cells (**Figure S9B**). By contrasting *in vivo* bioluminescence images to those obtained by both *in vivo* and *ex vivo* fluorescence imaging of RFP, it became clear that bioluminescence imaging greatly exaggerated tumor sizes, especially for low volumes of disease and at depth. Again, there was a poor correlation between either *in vivo* and *ex vivo* imaging of NIR-I emission from DiR with respect to RFP; but, there was a nearly identical correlation between the intensity and distribution of NIR-II emissive signals from core-shell nanoparticles with those of RFP fluorescence in the same organs. When assessing *in vivo* images obtained with different fluorescent channels, it was obvious that imaging of NIR-II emission from core-shell nanoparticles identified smaller and more numerous tumor deposits than could be observed by detection of RFP (**Figure 3B** and **S9C**); *in vivo* imaging of NIR-II emission from core-shell nanoparticles further afforded improved detection of individual tumor deposits as compared to *in vivo* imaging with all other reporters.

In addition to *in vivo* and *ex vivo* imaging experiments with mice, we examined the maximal depths of tissue penetration for emissive signals generated from each optical reporter used in our studies. A tumor implant that was isolated from the pancreas of our ovarian cancer mouse model was placed in a sample holder and was positioned at different depths beneath a tissue-like phantom, which was comprised of a synthetic polymer that exhibited optical properties for light absorption and scattering that mimicked those of the human breast. The maximum depth of tissue penetration for each optical reporter was denoted as the depth (i.e. the thickness of the phantom applied above the sample chamber) at which the signal-to-noise ratio (SNR) for detection decreased to 3. Analogous to the results obtained with *in vivo* imaging, the maximum depth of tissue penetration for each reporter correlated strongly with

its increasing wavelength of emission (**Figure 3C**); NIR-II emissive signals from core-shell nanoparticles were detectable at the deepest depths, penetrating a 20 mm-thick phantom.

Engineering Tumor Cell Uptake via FR Targeting. Flow cytometric analysis demonstrated high expression levels of FR on OVCAR-8 cells (**Figure 4A**). To generate an FR-targeted core-shell nanoparticle, we conjugated FA to amino-terminated PEO-b-PCL via EDC/NHS chemistry (see *Supplemental Material and Methods*). Integration of NMR peaks assigned to PEO (3.52 ppm) and FA (6.63, 7.6, and 8.653 ppm) verified the presence of 1:1 molar ratio of FA to PEO-b-PCL in the purified reaction product (**Figure S10**). DiR-Ho/Folate-PEO-PCL denotes FR-targeted nanoparticles that were comprised of a core of $NaYF_4$:Yb,Ho-based LNPs and a shell made up of a 1:9 molar ratio of FA-conjugated PEO_{6k}-PCL_{16k} to methoxy-PEO_{5k}-PCL_{16k}, which further incorporated DiR. The material and optical properties of these FR-targeted nanoparticles (DiR-Ho/Folate-PEO-PCL) were measured and summarized in **Figure S5** and **Table S1**. For *in vitro* experiments (*vide infra*), two other untargeted (DiL/PEO-PCL) and FR-targeted core-shell nanoparticles (DiL/Folate-PEO-PCL) were constructed that incorporated the DiR-related fluorophore DiL ($\lambda_{em\ max}$ = 575 nm).

We next verified the utility of FR-targeting to increase the accumulation of core-shell nanoparticles within LUC^+/RFP^{neg} OVCAR-8 cells grown in culture. The cells were incubated with either untargeted (DiL/PEO-PCL) or FR-targeted core-shell nanoparticles (DiL/Folate-PEO-PCL) for different time periods and washed; cellular accumulation was determined by flow cytometry, gating on DiL signals (**Figure 4B**). For both formulations, tumor cell accumulation increased over time but at a rate that was decidedly faster for the FR-targeted nanoparticles; indeed, by 6 h after incubation a marked increase in cellular accrual was already evident for FR-targeted (DiL/Folate-PEO-PCL) as compared to untargeted nanoparticles (DiL/PEO-PCL; **Figure 4C**). This result was further corroborated by cellular

imaging of LUC^+/RFP^+ OVCAR-8 cells that confirmed an increased uptake of FR-targeted nanoparticles (Er/Folate-PEO-PCL) with respect to untargeted nanoparticles (Er/PEO-PCL) after 6 h, visualizing visible RFP signals (red) and UC emission of core LNPs (green) by multiphoton confocal microscopy (**Figure 4D**). Cytotoxicity analyses of LUC^+/RFP^+ OVCAR-8 cells were also conducted at 72 h after incubation with various concentrations of either FR-targeted or untargeted core-shell nanoparticles. Cell viability was measured, which demonstrated a concentration-dependent toxicity for both formulations (**Figure S11**); the relatively enhanced cytotoxicity of FR-targeted nanoparticles was attributed to greater intracellular concentrations mediated by enhanced uptake. Note that neither nanoparticle formulation demonstrated significant *in vitro* toxicity to OVCAR-8 cells at concentrations that could be expected after *in vivo* administration (i.e. < 1 mg/mL). As such, the aforementioned nanoparticles were unlikely to affect the fidelity of *in vivo* imaging of cell intrinsic reporters (LUC and RFP), which were dependent upon preserved cellular viability.

The Route of Administration and the Role of FR-targeting on *In vivo* Tumor Accumulation of Core-shell Nanoparticles. LUC^+/RFP^+ OVCAR-8 tumor cells were xenotransplanted into nude mice via IP dissemination and allowed to grow for 2 weeks. Untargeted (DiR-Er/PEO-PCL) and FR-targeted core-shell nanoparticles (DiR-Ho/Folate-PEO-PCL) were then introduced by either IP (4 mice) or IV injection (4 mice). Simultaneous injection of both untargeted and FR-targeted nanoparticles into the same animal enabled ready comparisons of the effects of FR-targeting on the accuracy of tumor detection, the spatial contrast, and the maximal SNR that could be achieved via *in vivo* optical imaging with each emissive agent. **Figure 5A** (*upper row*) shows *in vivo* images of a single mouse at various time points after simultaneous IP administration of both nanoparticle formulations. Gross comparisons of the *ex vivo* images of excised organs taken at the time of animal sacrifice, which occurred at 72 h after nanoparticle administration, again demonstrated a high

correlation between RFP signals and the NIR-II emission of either the untargeted (Er) or FR-targeted nanoparticles (Ho).

Tumor deposits were easily visualized by all modalities (i.e. *ex vivo* RFP imaging or detection of NIR-II emission from Er and Ho) and were again found on the serosal surfaces of the ovaries (bilaterally), pancreas, duodenum, liver, spleen, stomach, and intestines. *Ex vivo* fluorescence signals from each excised organ were taken after animal sacrifice and were normalized to the intensity value obtained from the largest tumor deposit, which was on the pancreas of each animal; these normalized intensity values were then used to determine the relative biodistribution patterns for untargeted and FR-targeted core-shell nanoparticles after IP administration (**Figure 5B**). A close association was evident between the relative distribution of the RFP fluorescence and the NIR-II emission from both untargeted (Er) and FR-targeted nanoparticles (Ho).

From *in vivo* images taken longitudinally, it was apparent that a stable signal distribution pattern occurred for both the untargeted and FR-targeted nanoparticles at 10 h after IP administration (**Figures S12A** and **S12B**); both formulations were able to better visualize individual tumor deposits and to detect increased numbers of tumor implants as compared to *in vivo* imaging of RFP. Pharmacokinetic analyses were simultaneous conducted by taking small volume (typically 15 μL) blood draws at time points that corresponded to the *in vivo* images; measurements of NIR-II emission from Er (core LNPs) and NIR-I emission from DiR (in the PCL shell) enabled determination of the relative concentrations of each species in blood over time. Emission intensities were normalized to their highest values, yielding a half-life of clearance ($t_{1/2}$) of 12.5 $\pm$ 0.5 h (based on the NIR-II emission of Er) and 11.9 $\pm$ 0.2 h (based on NIR-I emission of DiR) for untargeted nanoparticles (**Figure S12C**). As such, monitoring of each optical channel yielded nearly identical blood clearance rates (p = 0.9704;

Student's *t*-test), establishing the *in vivo* stability of the core-shell structure after IP administration of the nanoparticles (**Figure 5C**, black circles).

IV administration of both untargeted and FR-targeted nanoparticles demonstrated a different distribution pattern to that which was seen after IP injection. **Figure 5A** (*lower row*) shows *in vivo* images of a single mouse at various time points after simultaneous IV administration of both formulations. Again, there was an apparent correlation between the *in vivo* images obtained by detection of each core-shell nanoparticle over time, demonstrating a stable biodistribution pattern at 10 h after IV injection (**Figure S12D**). Examination of *ex vivo* images taken of excised organs at the time of sacrifice, which, again, occurred at 72 h after nanoparticle injection, demonstrated a decreased correlation between the relative tissue distribution patterns of untargeted and FR-targeted core-shell nanoparticles that were introduced via this route (**Figure 5D** and **S12E**); additionally, the biodistribution pattern for either nanoparticle formulation did not seem to correspond with tumor locations visualized by *in vivo* or *ex vivo* imaging of RFP. The pharmacokinetic measurements based on NIR-II emission of Er and NIR-I emission of DiR were again similar after IV administration, demonstrating a $t_{1/2} = 11.4 \pm 0.6$ h (**Figure 5C**, red triangles, and **S12F**).

In order to accurately compare biodistribution patterns, we next sought to numerically correlate the relative intensities obtained by *ex vivo* imaging of NIR-II emission with those of RFP signals from harvested organs after IP administration of untargeted vs. FR-targeted core-shell nanoparticles. The results are depicted in **Figure 5E**, which contains diagonal plots that adopt the same fluorescence biodistribution patterns that are shown in **Figure 5B**. Each off-diagonal plot represents the correlation of a pair of fluorescent reporters, consisting of a linear-fit (red line), a value for the Pearson's correlation coefficient (r), and an adjusted R^2 value. The correlation between the RFP signal and either the NIR-II emission of untargeted

(Er) or FR-targeted core-shell nanoparticles (Ho) was very high: the distribution patterns of NIR-II signals from each nanoparticle formulation demonstrated an $r > 0.96$ with $R^2 > 0.90$ when compared to RFP. The correlation coefficient between RFP and DiR was, however, very poor ($r = 0.42$, $R^2 < 0.10$), demonstrating the inherent inaccuracies that result from identification of tumors by monitoring of NIR-I emission of DiR from these same core-shell nanoparticles (**Figure S12G**). Additionally, the correlation between untargeted and FR-targeted core-shell nanoparticles was nearly perfect with an $r > 0.99$ and $R^2 > 0.99$, demonstrating an identical pattern of tissue biodistribution (**Figures 5E** and **S12G**).

Histologic sections were made of excised tissues from separate animals that were similarly implanted with LUC^+/RFP^+ OVCAR-8 cells and imaged with either untargeted (Er/PEO-PCL; **Figure S8**) or FR-targeted core shell nanoparticles (Er/Folate-PEO-PCL) at 72 h after IP administration (**Figure S13**). When visualized via confocal microscopy, the untargeted and FR-targeted core-shell nanoparticles demonstrated identical patterns of tumor-specific accumulation with no evidence of healthy tissue uptake. Immuno-fluorescence was also performed for tumor-associated macrophages (TAMs) using FITC-conjugated F4/80 (green); tumor cells were detected by RFP emission (red) and core-shell nanoparticles were identified from their visible UC emission (blue; pseudo-color). Multifocal confocal microscopy demonstrated nanoparticle uptake by OVCAR-8 tumor cells (magenta) irrespective of FR-targeting (**Figures 5F** and **5G**, respectively). Taken together, these data supported that no further advantages in tumor targeting were afforded by conjugation of FA to nanoparticles introduced via the IP route of administration.

Enumeration of the *ex vivo* tissue distribution patterns for untargeted (Er) and FR-targeted core-shell nanoparticles (Ho) after IV administration revealed that they correlated poorly with those of the tumor deposits (RFP), yielding an $r = 0.20$ ($R^2 < 0.1$), 0.16 ($R^2 < 0.1$), and 0.26

($R^2 < 0.1$) for the association of RFP with DiR (NIR-I), Er (NIR-II) and Ho (NIR-II) signals, respectively (**Figure S14**). Both untargeted and FR-targeted nanoparticles demonstrated a pattern of predominantly liver and splenic accumulation, corresponding to organs of known reticuloendothelial cell activity and nanoparticle uptake. These results were confirmed by fluorescence imaging of histologic tissue sections (**Figure S15** and **S16**). On closer examination, the association between the signals from untargeted (Er) and FR-targeted nanoparticles (Ho) was also lower after IV administration, yielding an $r = 0.8$ ($R^2 = 0.6$; **Figure S14**); this was attributed to a relatively larger but variable degree of lung accumulation for FR-targeted core-shell nanoparticles. Immunostaining demonstrated the presence of TAMs (green) near LUC^+/RFP^+ OVCAR-8 tumor cells (red); the intratumoral distributions of both untargeted (Er/PEO-PCL) and FR-targeted nanoparticles (Er/Folate-PEO-PCL; blue), however, did not clearly indicate a particular cellular tropism (**Figure S17**).

Early Detection of Tumor Deposits at 1 week after Implantation. Nude mice were xenotransplanted with LUC^+/RFP^+ OVCAR-8 cells and untargeted core-shell nanoparticles (DiR-Er/PEO-PCL) were administered by IP injection at 1 week after tumor cell implantation. Animals were imaged over a period of 72 h and their organs were excised in order to compare the relative intensities and tissue distribution patterns of NIR-I signals from DiR, NIR-II fluorescence from core LNPs (Er) and RFP (**Figure 6**). Comparisons of *ex vivo* images, again, readily demonstrated a strong correlation between NIR-II emissive signals (Er) and RFP localization; *in vivo* imaging confirmed the superiority of monitoring of NIR-II emission to detect numerous early tumor deposits within these animals, demonstrating increased sensitivity and improved spatial contrast as compared to imaging of RFP (**Figure 6A**).

For each reporter, the fluorescence intensities from various organs were, again, normalized to that of the largest tumor deposit, which was on the pancreas of each animal (**Figure 6B**). A correlation matrix was similarly obtained by comparing the biodistribution patterns of all

three emissive signals (RFP, DiR and Er) and was used to further quantify the ability of each extrinsic reporter to detect early tumor deposits, which were delineated by RFP fluorescence (**Figure 6C**). Correlation of RFP signals with NIR-I emission from DiR was particularly poor (r = 0.20, R^2 < 0.10); NIR-II emission from Er also demonstrated a weaker correlation with RFP fluorescence in excised organs from these 1-week old xenotransplants (r > 0.80, R^2 > 0.60), especially when compared to results obtained at two weeks after tumor cell implantation (r > 0.96, R^2 > 0.92). Note that the intensity of RFP fluorescence was much weaker in these early tumor deposits, which correlated to a decreased SNR when imaging with this intrinsic reporter. As a result, *in vivo* and *ex vivo* optical imaging of RFP fluorescence in excised organs demonstrated a diminished ability to correctly identify tumor implants that were confirmed by multiphoton confocal microscopy of RFP fluorescence in histologic sections. These microscopic tumor deposits corresponded to organs that demonstrated high NIR-II emission on *ex vivo* imaging; NIR-II signals from these same organs were also visualized by *in vivo* imaging, demonstrating the improved detection sensitivity that was afford by utilizing NIR-II fluorescence as compared to that of RFP in order to identify early tumor deposits within these animals.

DISCUSSION

Intrinsic reporters such as RFP and LUC have been commonly utilized to visualize tumors, to follow their growth, and to monitor their therapeutic responses in whole-animal imaging studies. *In vivo* bioluminescence imaging, however, has been constrained by: 1) the short lifetime of the enzyme-substrate reaction, which has necessitated re-dosing and which has decreased the frequency at which longitudinal studies may be conducted; 2) non-uniform diffusion of the luciferin substrate and its inaccessibility to necrotic portions of a tumor; and, 3) substantial light scattering at depth, which has resulted in inaccurate estimations of tumor volumes [65]. Conversely, *in vivo* RFP imaging has obviated many of these aforementioned

limitations; but, the absolute magnitude of the RFP signal has not correlated with tumor burden due to nonlinear optical scattering and biological absorbance, which have further hindered the accuracy of tumor detection with increasing depth [65]. As *in vivo* optical imaging with various NIR-I and NIR-II emissive agents has been proposed to circumvent these challenges [66, 67], we undertook a comparative study to establish the fidelity of the *in vivo* imaging results obtained by detection of each of these intrinsic and extrinsic reporters.

Oleic acid-modified LNPs were coated with amphiphilic diblock copolymers of PEO-b-PCL through optimization of an aqueous dispersion method [68]. These core-shell nanoparticles further encapsulated the organic fluorophore DiR in their PCL shells, which demonstrated improved photostability as compared to its emission in bulk solution. Note that similar phenomenona have been observed in other studies that have examined the emission of fluorophores in immobilized polymeric membranes and in nanoparticles [69-72]; they are likely attributable to multiple factors, including reduced concentrations of oxygen and nucleophiles, more efficient dissipation of heat following absorption and emission/internal conversion, as well as the restriction in the population of conformations that are present in the excited state or hot ground state of fluorophores in polymeric environments as compared to when in bulk solution. As a result, the core-shell nanoparticles were found to generate stable visible, NIR-I, and NIR-II emissive signals, which facilitated correlative whole animal and tissue-level experiments.

Two weeks after peritoneal dissemination of LUC^+/RFP^+ OVCAR-8 cells in nude mice, *ex vivo* imaging confirmed a nearly perfect association between the biodistribution patterns of peritoneal tumor implants (RFP) with those of the core-shell nanoparticles (NIR-II emissive signals) that were introduced by IP administration. Both *ex vivo* and *in vivo* imaging of NIR-II fluorescence demonstrated superior sensitivity and improved spatial resolution as compared to

detection of either NIR-I emission from DiR or NIR-I UC fluorescence from the same nanoparticles. The particularly poor correlation between the biodistribution patterns observed for DiR as compared to RFP may be attributable to the leakge of the organic fluorophore from the core-shell nanoparticles at longer time scales, which would limit the achieveable SNR and prevent the accurate detection of smaller, earlier-stage, and deeper tumor implants. *In vivo* imaging of NIR-II emission uniquely enabled the visualization of individual tumor deposits, detecting all microscopically-confirmed tumors and at substantially deeper depths of tissue penetration than could be obtained by monitoring of the NIR-I fluorescence of DiR or that of the cell intrinsic reporters (LUC or RFP). These advantages further enabled the earlier detection of tumors, which were imaged at 1 week after implantation; *in vivo* imaging of NIR-II fluorescence again proved superior at identifying all tumor locations, visualizing numerous minute deposits that were not otherwise identified.

Although core-shell nanoparticles were highly localized to *in vivo* tumor locations after IP administration, we also explored the role of a tumor-targeting agent to further improve the SNR for *in vivo* imaging. The FR has been shown to be a highly expressed and validated target for clinical ovarian cancer therapy [57, 58]; and, conjugation of the small molecule FA to various imaging agents has previously enabled accurate detection of epithelial ovarian cancers in both preclinical and clinical studies [59]. Here, FR-targeted core-shell nanoparticles were generated from FA-conjugated PEO-b-PCL polymers; their materials and optical properties were validated; and, their enhanced *in vitro* uptake by FR-expressing OVCAR-8 cells was observed by flow cytometry and by confocal microscopy.

In vivo optical imaging of two separate nanoparticles with spectrally unique NIR-II emissive signatures enabled independent tracking of each formulation within a single animal after simultaneous administration. When introduced by IP injection at 2 weeks after tumor cell

implantation, the biodistribution pattern of the FR-targeted core-shell nanoparticle was found to be identical to that of its untargeted counterpart, which showed a nearly perfect correlation with tumor locations (RFP distribution). Indeed, *in vivo* imaging of NIR-II fluorescence confirmed that IP injection of untargeted core-shell nanoparticles was sufficient to enable preferential uptake in tumor tissues even at 1 week after tumor cell implantation, demonstrating increased sensitivity and improved spatial contrast as compared to utilizing intrinsic RFP signals to identify these early stage tumors. Note that there was a poor correlation between the relative tissue biodistribution patterns of untargeted and FR-targeted core-shell nanoparticles after IV injection, demonstrating no discernable tumor-specific targeting or intratumoral cellular tropism. As such, while FA conjugation to nanoparticles definitively aided *in vitro* tumor cell uptake, the results presented here indicate that no further advantages for *in vivo* tumor targeting were achieved.

To our knowledge, PEGylated and untargeted nanoparticles have not been shown to demonstrate this high degree of tumor specificity after IP administration; and, the mechanisms underlying their accumulation are unknown. As previous investigators have noted that human epithelial ovarian cancers possess large numbers of TAMs [73], we hypothesized that intraperitoneal uptake by these macrophages and their subsequent homing to tumor sites could account for nanoparticle accretion. Immunofluorescence staining of TAMs was performed in excised tumor tissues; the tumors were imaged by multiphoton confocal microscopy; and, the locations of core-shell nanoparticles (with respect to TAMs and RFP^{+} OVCAR-8 ovarian cancer cells) were observed from the visible UC emission of their core LNPs. No clear cellular association patterns for either untargeted or FR-targeted core-shell nanoparticles were determined. As such, the mechanisms of tumor uptake for these PEGylated nanoparticles after IP injection remain unknown and warrant further investigation. If confirmed in other studies, IP administration of nanoparticles may be exploited to improve ovarian cancer

imaging and therapy. Finally, the results presented here validate a generalizable paradigm in which whole-animal optical imaging at NIR-II wavelengths may be used to accurately monitor multiple nanoparticle populations, thereby enabling simultaneous examinations of both experimental and control formulations under identical *in vivo* conditions.

CONCLUSIONS

We have demonstrated that *in vivo* optical imaging of NIR-II fluorescence was able to accurately identify minute and early tumor deposits that were otherwise missed by detection of exogenous NIR-I emissive agents or intrinsic LUC and RFP reporters. Simultaneous NIR-II excitation (980 nm) of two different nanoparticle compositions that possessed non-overlapping NIR-II emission maxima (1566 and 1162 nm) enabled independent tracking of each formulation after concurrent administration. To our knowledge, such direct, highly sensitive, and longitudinal *in vivo* optical imaging comparisons between experimental and control formulations have not previously been rigorously demonstrated in the same animal. Our results have identified the advantages of IP as opposed to IV administration of nanoparticles and have called into question the utility of small molecule targeting agents to further enable their accumulation within peritoneal tumor deposits. Adoption of our methods may facilitate the preclinical development of other diagnostic and therapeutic constructs based on direct *in vivo* comparisons enabled by NIR-II optical imaging.

ABBREVIATIONS

1,1'-dioctadecyl-3,3,3',3'-tetramethylindotricarbocyanine iodide (DiR); DiR-encapsulated PEO_{5k}-PCL_{16k}-coated $NaYF_4$:Yb,Er,Tm-based LNPs (DiR-Er,Tm/PEO-PCL); DiR-encapsulated PEO_{5k}-PCL_{16k}-coated $NaYF_4$:Yb,Er-based LNPs (DiR-Er/PEO-PCL); DiR-encapsulated, FA-conjugated, PEO_{6k}-PCL_{16k}-coated $NaYF_4$:Yb,Ho-based LNPs (DiR-Ho/Folate-PEO-PCL); dynamic light scattering (DLS); erbium (Er); indium gallium arsenide

(InGaAs); intraperitoneal (IP); intravenous (IV); lanthanide nanoparticles (LNPs); luciferase (LUC); near-infrared (NIR); polydispersity index (PDI); poly(ethylene oxide)-block-poly(ε-caprolactone) (PEO-b-PCL); red fluorescent protein (RFP); sodium yttrium fluoride ($NaYF_4$); thulium (Tm); up-conversion (UC); ytterbium (Yb); holmium (Ho);

SUPPORTING INFORMATION

Supporting Information is available online or from the authors.

AUTHOR CONTRIBUTIONS

ZT and XD contributed to the design of the research study, conducted experiments, acquired and analyzed data, and helped to write the manuscript. XH conducted experiments and aided in the acquisition of data. MM contributed to the design of the research study, aided in data acquisition and analysis, and provided reagents. ESX and NMB aided in acquiring and analyzing data. HS, RQ, and YY conducted experiments and aided in the acquisition of data. TL, WW, and JW aided in data acquisition and analyses. MJB contributed to the design of the research study and provided reagents. AMB and PPG contributed to the design of the research study, the analysis of the data, and wrote the manuscript.

ACKNOWLEDGEMENTS

This work was partially supported by a 2014 Koch Institute Frontiers Research Grant (AMB and PPG) as well as by an Amgen Research Grant from the Foundation for Women's Cancer (PPG). ZT is thankful for the generous support of the Misrock Foundation. PPG acknowledges further support from the Charles W. and Jennifer C. Johnson Clinical Investigator Fund and from the Kathryn Fox Samway Foundation. N.M.B. would like to acknowledge support through a 2016 Misrock Postdoctoral Fellowship Award.

REFERENCES

[1] J. Rao, A. Dragulescu-Andrasi, H. Yao, Fluorescence imaging in vivo: recent advances, Curr Opin Biotechnol 18(1) (2007) 17-25.
[2] V. Ntziachristos, Fluorescence molecular imaging, Annu Rev Biomed Eng 8 (2006) 1-33.
[3] R. Weissleder, M.J. Pittet, Imaging in the era of molecular oncology, Nature 452(7187) (2008) 580-589.
[4] S. Diao, G. Hong, A. Antaris, J. Blackburn, K. Cheng, Z. Cheng, H. Dai, Biological imaging without autofluorescence in the second near-infrared region, Nano Res. 8(9) (2015) 3027-3034.
[5] A.M. Smith, M.C. Mancini, S. Nie, Bioimaging: second window for in vivo imaging, Nature nanotechnology 4(11) (2009) 710-1.
[6] D. Ghosh, A.F. Bagley, Y.J. Na, M.J. Birrer, S.N. Bhatia, A.M. Belcher, Deep, noninvasive imaging and surgical guidance of submillimeter tumors using targeted M13-stabilized single-walled carbon nanotubes, Proceedings of the National Academy of Sciences of the United States of America 111(38) (2014) 13948-53.
[7] N.M. Bardhan, D. Ghosh, A.M. Belcher, Carbon nanotubes as in vivo bacterial probes, Nat Commun 5 (2014).
[8] A.L. Antaris, H. Chen, K. Cheng, Y. Sun, G. Hong, C. Qu, S. Diao, Z. Deng, X. Hu, B. Zhang, X. Zhang, O.K. Yaghi, Z.R. Alamparambil, X. Hong, Z. Cheng, H. Dai, A small-molecule dye for NIR-II imaging, Nat Mater 15(2) (2016) 235-242.
[9] G. Hong, Y. Zou, A.L. Antaris, S. Diao, D. Wu, K. Cheng, X. Zhang, C. Chen, B. Liu, Y. He, J.Z. Wu, J. Yuan, B. Zhang, Z. Tao, C. Fukunaga, H. Dai, Ultrafast fluorescence imaging in vivo with conjugated polymer fluorophores in the second near-infrared window, Nat Commun 5 (2014) 4206.
[10] Z. Tao, G. Hong, C. Shinji, C. Chen, S. Diao, A.L. Antaris, B. Zhang, Y. Zou, H. Dai, Biological imaging using nanoparticles of small organic molecules with fluorescence emission at wavelengths longer than 1000 nm, Angewandte Chemie 52(49) (2013) 13002-6.
[11] K. Welsher, Z. Liu, D. Daranciang, H. Dai, Selective probing and imaging of cells with single walled carbon nanotubes as near-infrared fluorescent molecules, Nano letters 8(2) (2008) 586-90.
[12] K. Welsher, Z. Liu, S.P. Sherlock, J.T. Robinson, Z. Chen, D. Daranciang, H. Dai, A route to brightly fluorescent carbon nanotubes for near-infrared imaging in mice, Nature nanotechnology 4(11) (2009) 773-80.
[13] K. Welsher, S.P. Sherlock, H. Dai, Deep-tissue anatomical imaging of mice using carbon nanotube fluorophores in the second near-infrared window, Proceedings of the National Academy of Sciences of the United States of America 108(22) (2011) 8943-8.
[14] G. Hong, J.C. Lee, J.T. Robinson, U. Raaz, L. Xie, N.F. Huang, J.P. Cooke, H. Dai, Multifunctional in vivo vascular imaging using near-infrared II fluorescence, Nature medicine 18(12) (2012) 1841-6.
[15] H. Kosuge, S.P. Sherlock, T. Kitagawa, R. Dash, J.T. Robinson, H. Dai, M.V. McConnell, Near infrared imaging and photothermal ablation of vascular inflammation using single-walled carbon nanotubes, Journal of the American Heart Association 1(6) (2012) e002568.
[16] G. Hong, J.C. Lee, A. Jha, S. Diao, K.H. Nakayama, L. Hou, T.C. Doyle, J.T. Robinson, A.L. Antaris, H. Dai, J.P. Cooke, N.F. Huang, Near-infrared II fluorescence for imaging hindlimb vessel regeneration with dynamic tissue perfusion measurement, Circulation. Cardiovascular imaging 7(3) (2014) 517-25.
[17] H. Yi, D. Ghosh, M.H. Ham, J. Qi, P.W. Barone, M.S. Strano, A.M. Belcher, M13 phage-functionalized single-walled carbon nanotubes as nanoprobes for second near-infrared window fluorescence imaging of targeted tumors, Nano letters 12(3) (2012) 1176-83.

[18] S. Diao, G. Hong, J.T. Robinson, L. Jiao, A.L. Antaris, J.Z. Wu, C.L. Choi, H. Dai, Chirality enriched (12,1) and (11,3) single-walled carbon nanotubes for biological imaging, Journal of the American Chemical Society 134(41) (2012) 16971-4.
[19] A.L. Antaris, J.T. Robinson, O.K. Yaghi, G. Hong, S. Diao, R. Luong, H. Dai, Ultra-low doses of chirality sorted (6,5) carbon nanotubes for simultaneous tumor imaging and photothermal therapy, ACS nano 7(4) (2013) 3644-52.
[20] S. Diao, J.L. Blackburn, G. Hong, A.L. Antaris, J. Chang, J.Z. Wu, B. Zhang, K. Cheng, C.J. Kuo, H. Dai, Fluorescence Imaging In Vivo at Wavelengths beyond 1500 nm, Angewandte Chemie (2015).
[21] Y. Zhang, Y. Zhang, G. Hong, W. He, K. Zhou, K. Yang, F. Li, G. Chen, Z. Liu, H. Dai, Q. Wang, Biodistribution, pharmacokinetics and toxicology of Ag2S near-infrared quantum dots in mice, Biomaterials 34(14) (2013) 3639-46.
[22] Y. Zhang, G. Hong, Y. Zhang, G. Chen, F. Li, H. Dai, Q. Wang, Ag2S quantum dot: a bright and biocompatible fluorescent nanoprobe in the second near-infrared window, ACS nano 6(5) (2012) 3695-702.
[23] C. Li, Y. Zhang, M. Wang, Y. Zhang, G. Chen, L. Li, D. Wu, Q. Wang, In vivo real-time visualization of tissue blood flow and angiogenesis using Ag2S quantum dots in the NIR-II window, Biomaterials 35(1) (2014) 393-400.
[24] G. Chen, F. Tian, C. Li, Y. Zhang, Z. Weng, Y. Zhang, R. Peng, Q. Wang, In vivo real-time visualization of mesenchymal stem cells tropism for cutaneous regeneration using NIR-II fluorescence imaging, Biomaterials 53 (2015) 265-73.
[25] C.N. Zhu, P. Jiang, Z.L. Zhang, D.L. Zhu, Z.Q. Tian, D.W. Pang, Ag(2)Se quantum dots with tunable emission in the second near-infrared window, ACS applied materials & interfaces 5(4) (2013) 1186-9.
[26] D.J. Naczynski, C. Sun, S. Turkcan, C. Jenkins, A.L. Koh, D. Ikeda, G. Pratx, L. Xing, X-ray-induced shortwave infrared biomedical imaging using rare-earth nanoprobes, Nano letters 15(1) (2015) 96-102.
[27] D.J. Naczynski, M.C. Tan, M. Zevon, B. Wall, J. Kohl, A. Kulesa, S. Chen, C.M. Roth, R.E. Riman, P.V. Moghe, Rare-earth-doped biological composites as in vivo shortwave infrared reporters, Nat Commun 4 (2013) 2199.
[28] M. Pokhrel, L.C. Mimun, B. Yust, G.A. Kumar, A. Dhanale, L. Tang, D.K. Sardar, Stokes emission in GdF(3):Nd(3)(+) nanoparticles for bioimaging probes, Nanoscale 6(3) (2014) 1667-74.
[29] G. Chen, T.Y. Ohulchanskyy, S. Liu, W.C. Law, F. Wu, M.T. Swihart, H. Agren, P.N. Prasad, Core/shell NaGdF4:Nd(3+)/NaGdF4 nanocrystals with efficient near-infrared to near-infrared downconversion photoluminescence for bioimaging applications, ACS nano 6(4) (2012) 2969-77.
[30] L. Sun, X. Ge, J. Liu, Y. Qiu, Z. Wei, B. Tian, L. Shi, Multifunctional nanomesoporous materials with upconversion (in vivo) and downconversion (in vitro) luminescence imaging based on mesoporous capping UCNPs and linking lanthanide complexes, Nanoscale 6(21) (2014) 13242-52.
[31] S. Sivakumar, P.R. Diamente, F.C. van Veggel, Silica-coated Ln3+-Doped LaF3 nanoparticles as robust down- and upconverting biolabels, Chemistry 12(22) (2006) 5878-84.
[32] M. Kamimura, T. Matsumoto, S. Suyari, M. Umezawa, K. Soga, Ratiometric near-infrared fluorescence nanothermometry in the OTN-NIR (NIR II/III) biological window based on rare-earth doped β-NaYF4 nanoparticles, J. Mater. Chem. B 5(1917) (2017).
[33] Y. Jung, S. Jeong, W. Nayoun, B. Ahn, J. Kwag, S. Geol Kim, S. Kim, Quantum dot imaging in the second near-infrared optical window: studies on reflectance fluorescence imaging depths by effective fluence rate and multiple image acquisition, Journal of biomedical optics 20(4) (2015) 46012.

[34] M. Haase, K. Riwotzki, H. Meyssamy, A. Kornowski, Synthesis and properties of colloidal lanthanide-doped nanocrystals, Journal of Alloys and Compounds 303 (2000) 191-197.
[35] F. Wang, X. Liu, Recent advances in the chemistry of lanthanide-doped upconversion nanocrystals, Chemical Society reviews 38(4) (2009) 976-89.
[36] A. Sedlmeier, H.H. Gorris, Surface modification and characterization of photon-upconverting nanoparticles for bioanalytical applications, Chemical Society reviews 44(6) (2015) 1526-60.
[37] D. Yang, P. Ma, Z. Hou, Z. Cheng, C. Li, J. Lin, Current advances in lanthanide ion (Ln(3+))-based upconversion nanomaterials for drug delivery, Chemical Society reviews 44(6) (2015) 1416-48.
[38] P. Huang, W. Zheng, S. Zhou, D. Tu, Z. Chen, H. Zhu, R. Li, E. Ma, M. Huang, X. Chen, Lanthanide-doped LiLuF(4) upconversion nanoprobes for the detection of disease biomarkers, Angewandte Chemie 53(5) (2014) 1252-7.
[39] D.J. Naczynski, M.C. Tan, R.E. Riman, P.V. Moghe, Rare Earth Nanoprobes for Functional Biomolecular Imaging and Theranostics, Journal of materials chemistry. B, Materials for biology and medicine 2(20) (2014) 2958-2973.
[40] S.P. Fricker, The therapeutic application of lanthanides, Chemical Society reviews 35(6) (2006) 524-33.
[41] G. Chen, H. Qiu, P.N. Prasad, X. Chen, Upconversion nanoparticles: design, nanochemistry, and applications in theranostics, Chemical reviews 114(10) (2014) 5161-214.
[42] W. Feng, C. Han, F. Li, Upconversion-nanophosphor-based functional nanocomposites, Advanced materials 25(37) (2013) 5287-303.
[43] Z. Gu, L. Yan, G. Tian, S. Li, Z. Chai, Y. Zhao, Recent advances in design and fabrication of upconversion nanoparticles and their safe theranostic applications, Advanced materials 25(28) (2013) 3758-79.
[44] C. Wang, L. Cheng, Z. Liu, Upconversion nanoparticles for photodynamic therapy and other cancer therapeutics, Theranostics 3(5) (2013) 317-30.
[45] L. Cheng, C. Wang, Z. Liu, Upconversion nanoparticles and their composite nanostructures for biomedical imaging and cancer therapy, Nanoscale 5(1) (2013) 23-37.
[46] J. Zhou, Z. Liu, F. Li, Upconversion nanophosphors for small-animal imaging, Chemical Society reviews 41(3) (2012) 1323-49.
[47] D.K. Chatterjee, M.K. Gnanasammandhan, Y. Zhang, Small upconverting fluorescent nanoparticles for biomedical applications, Small 6(24) (2010) 2781-95.
[48] G. Wang, Q. Peng, Y. Li, Lanthanide-doped nanocrystals: synthesis, optical-magnetic properties, and applications, Accounts of chemical research 44(5) (2011) 322-32.
[49] Y. Liu, D. Tu, H. Zhu, X. Chen, Lanthanide-doped luminescent nanoprobes: controlled synthesis, optical spectroscopy, and bioapplications, Chemical Society reviews 42(16) (2013) 6924-58.
[50] W. Qi, P.P. Ghoroghchian, G. Li, D.A. Hammer, M.J. Therien, Aqueous self-assembly of poly(ethylene oxide)-block-poly(epsilon-caprolactone) (PEO-b-PCL) copolymers: disparate diblock copolymer compositions give rise to nano- and meso-scale bilayered vesicles, Nanoscale 5(22) (2013) 10908-15.
[51] S.M. Moghimi, J. Szebeni, Stealth liposomes and long circulating nanoparticles: critical issues in pharmacokinetics, opsonization and protein-binding properties, Progress in lipid research 42(6) (2003) 463-78.
[52] Y. Geng, D.E. Discher, Hydrolytic degradation of poly(ethylene oxide)-block-polycaprolactone worm micelles, Journal of the American Chemical Society 127(37) (2005) 12780-1.

[53] H. Cho, G.L. Indig, J. Weichert, H.C. Shin, G.S. Kwon, In vivo cancer imaging by poly(ethylene glycol)-b-poly(varepsilon-caprolactone) micelles containing a near-infrared probe, Nanomedicine : nanotechnology, biology, and medicine 8(2) (2012) 228-36.
[54] D.A. Christian, S. Cai, O.B. Garbuzenko, T. Harada, A.L. Zajac, T. Minko, D.E. Discher, Flexible filaments for in vivo imaging and delivery: persistent circulation of filomicelles opens the dosage window for sustained tumor shrinkage, Molecular pharmaceutics 6(5) (2009) 1343-52.
[55] Y. Urano, M. Sakabe, N. Kosaka, M. Ogawa, M. Mitsunaga, D. Asanuma, M. Kamiya, M.R. Young, T. Nagano, P.L. Choyke, H. Kobayashi, Rapid cancer detection by topically spraying a gamma-glutamyltranspeptidase-activated fluorescent probe, Science translational medicine 3(110) (2011) 110ra119.
[56] A.K. Mitra, D.A. Davis, S. Tomar, L. Roy, H. Gurler, J. Xie, D.D. Lantvit, H. Cardenas, F. Fang, Y. Liu, E. Loughran, J. Yang, M. Sharon Stack, R.E. Emerson, K.D. Cowden Dahl, V.B. M, K.P. Nephew, D. Matei, J.E. Burdette, In vivo tumor growth of high-grade serous ovarian cancer cell lines, Gynecologic oncology 138(2) (2015) 372-7.
[57] G. Toffoli, C. Cernigoi, A. Russo, A. Gallo, M. Bagnoli, M. Boiocchi, Overexpression of folate binding protein in ovarian cancers, International journal of cancer. Journal international du cancer 74(2) (1997) 193-8.
[58] N. Parker, M.J. Turk, E. Westrick, J.D. Lewis, P.S. Low, C.P. Leamon, Folate receptor expression in carcinomas and normal tissues determined by a quantitative radioligand binding assay, Analytical biochemistry 338(2) (2005) 284-93.
[59] I.B. Vergote, C. Marth, R.L. Coleman, Role of the folate receptor in ovarian cancer treatment: evidence, mechanism, and clinical implications, Cancer metastasis reviews 34(1) (2015) 41-52.
[60] Z. Chen, H. Chen, H. Hu, M. Yu, F. Li, Q. Zhang, Z. Zhou, T. Yi, C. Huang, Versatile synthesis strategy for carboxylic acid-functionalized upconverting nanophosphors as biological labels, Journal of the American Chemical Society 130(10) (2008) 3023-9.
[61] X. Wang, J. Zhuang, Q. Peng, Y. Li, A general strategy for nanocrystal synthesis, Nature 437(7055) (2005) 121-4.
[62] B. Zhou, B. Shi, D. Jin, X. Liu, Controlling upconversion nanocrystals for emerging applications, Nature nanotechnology 10(11) (2015) 924-36.
[63] X. Li, J. Zhu, Z. Man, Y. Ao, H. Chen, Investigation on the structure and upconversion fluorescence of Yb(3)(+)/Ho(3)(+) co-doped fluorapatite crystals for potential biomedical applications, Sci Rep 4 (2014) 4446.
[64] E. Lengyel, Ovarian cancer development and metastasis, Am J Pathol 177(3) (2010) 1053-64.
[65] J. Condeelis, R. Weissleder, In vivo imaging in cancer, Cold Spring Harbor perspectives in biology 2(12) (2010) a003848.
[66] J.V. Frangioni, In vivo near-infrared fluorescence imaging, Current opinion in chemical biology 7(5) (2003) 626-34.
[67] S.A. Hilderbrand, R. Weissleder, Near-infrared fluorescence: application to in vivo molecular imaging, Current opinion in chemical biology 14(1) (2010) 71-9.
[68] Z. Wu, C. Guo, S. Liang, H. Zhang, L. Wang, H. Sun, B. Yang, A pluronic F127 coating strategy to produce stable up-conversion NaYF4:Yb,Er(Tm) nanoparticles in culture media for bioimaging, Journal of Materials Chemistry 22(35) (2012) 18596-18602.
[69] P.P. Ghoroghchian, P.R. Frail, K. Susumu, T.H. Park, S.P. Wu, H.T. Uyeda, D.A. Hammer, M.J. Therien, Broad spectral domain fluorescence wavelength modulation of visible and near-infrared emissive polymersomes, Journal of the American Chemical Society 127(44) (2005) 15388-90.
[70] P.P. Ghoroghchian, P.R. Frail, K. Susumu, D. Blessington, A.K. Brannan, F.S. Bates, B. Chance, D.A. Hammer, M.J. Therien, Near-infrared-emissive polymersomes: self-assembled

soft matter for in vivo optical imaging, Proceedings of the National Academy of Sciences of the United States of America 102(8) (2005) 2922-7.
[71] T.V. Duncan, P.P. Ghoroghchian, I.V. Rubtsov, D.A. Hammer, M.J. Therien, Ultrafast excited-state dynamics of nanoscale near-infrared emissive polymersomes, Journal of the American Chemical Society 130(30) (2008) 9773-84.
[72] P.P. Lima, M.M. Nolasco, F.A.A. Paz, R.A.S. Ferreira, R.L. Longo, O.L. Malta, L.D. Carlos, Photo–Click Chemistry to Design Highly Efficient Lanthanide β-Diketonate Complexes Stable under UV Irradiation, Chem. Mater. 25(4) (2013) 586-598.
[73] E.K. Colvin, Tumor-associated macrophages contribute to tumor progression in ovarian cancer, Frontiers in oncology 4 (2014) 137.

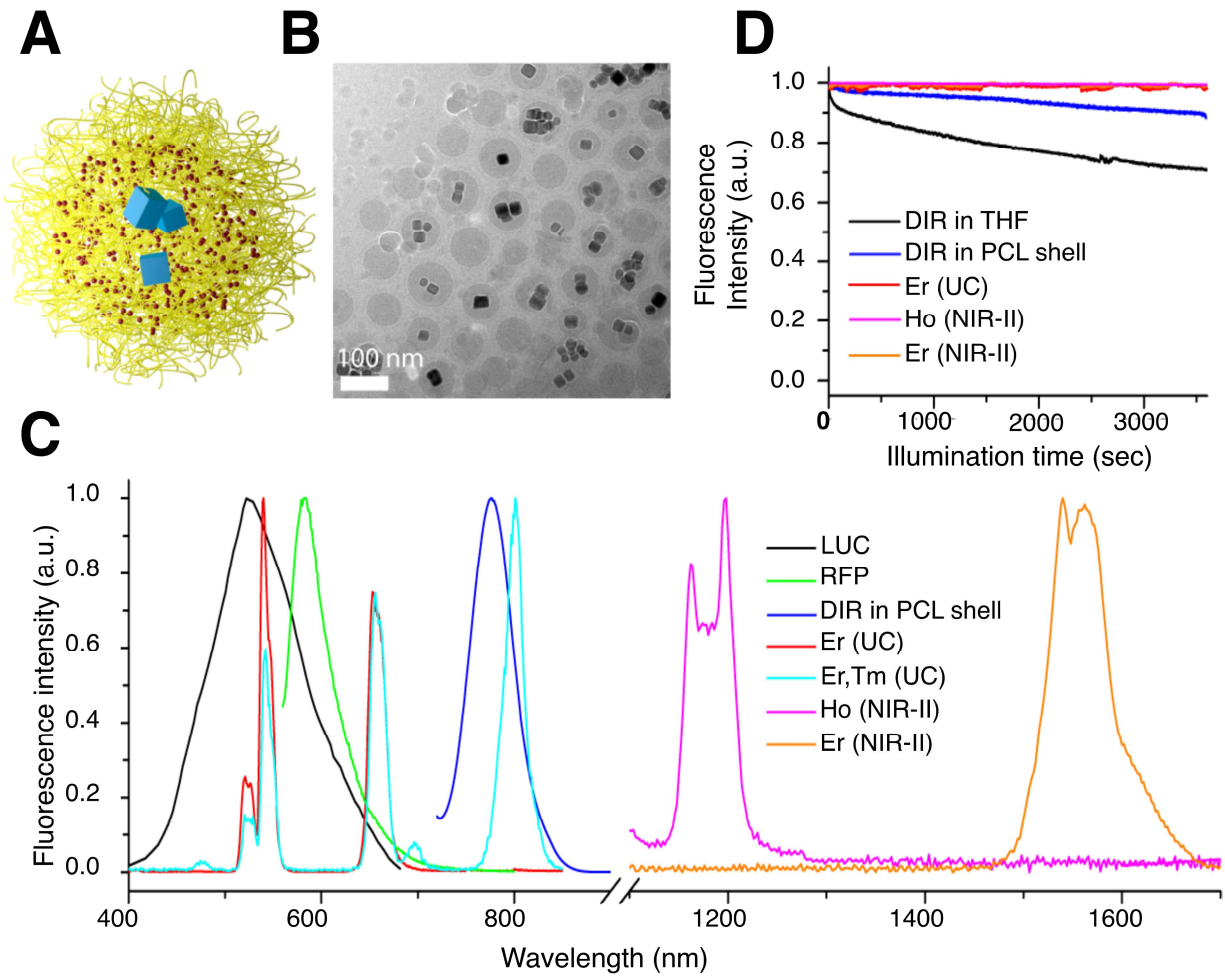

Figure 1. Structural and optical characterization of core-shell nanoparticles. A) Illustration depicting core-shell nanoparticles comprised of PEO-b-PCL diblock copolymers (yellow), the organic NIR-I fluorophore DiR (red), and LNPs (blue). B) Cryo-TEM image of core-shell nanoparticles (DiR-Er/PEO-PCL) in aqueous suspension (scale bar = 100 nm). C) Normalized fluorescence spectra of intrinsic reports (LUC and RFP) as well as emissive components of various core-shell nanoparticle formulations. 980-nm laser-excitation of DiR-Er/PEO-PCL resulted in up-conversion emission (Er (UC); red) and NIR-II fluorescence (Er (NIR-II); orange) from core $NaYF_4$:Yb,Er-based LNPs; 700-nm irradiation of the same particles resulted in NIR-I emission from DiR (DiR; navy blue) in their PCL shells. 980-nm irradiation of DiR-Er,Tm/PEO-PCL resulted in UC emission (Er,Tm (UC); cyan) from core $NaYF_4$:Yb,Er,Tm-based LNPs; similar excitation of DiR-Ho/Folate-PEO-PCL resulted in both UC emission and NIR-II fluorescence (Ho (NIR-II); magenta) from core $NaYF_4$:Yb,Ho-based LNPs. D) Measurements of the photostability of various emissive components of core-shell nanoparticles under continuous irradiation. Note that the same excitation energies were utilized as in C; and, emission was detected using various excitation and emission filters. The photostability of DiR in THF (DiR in THF; black) was included for comparative purposes.

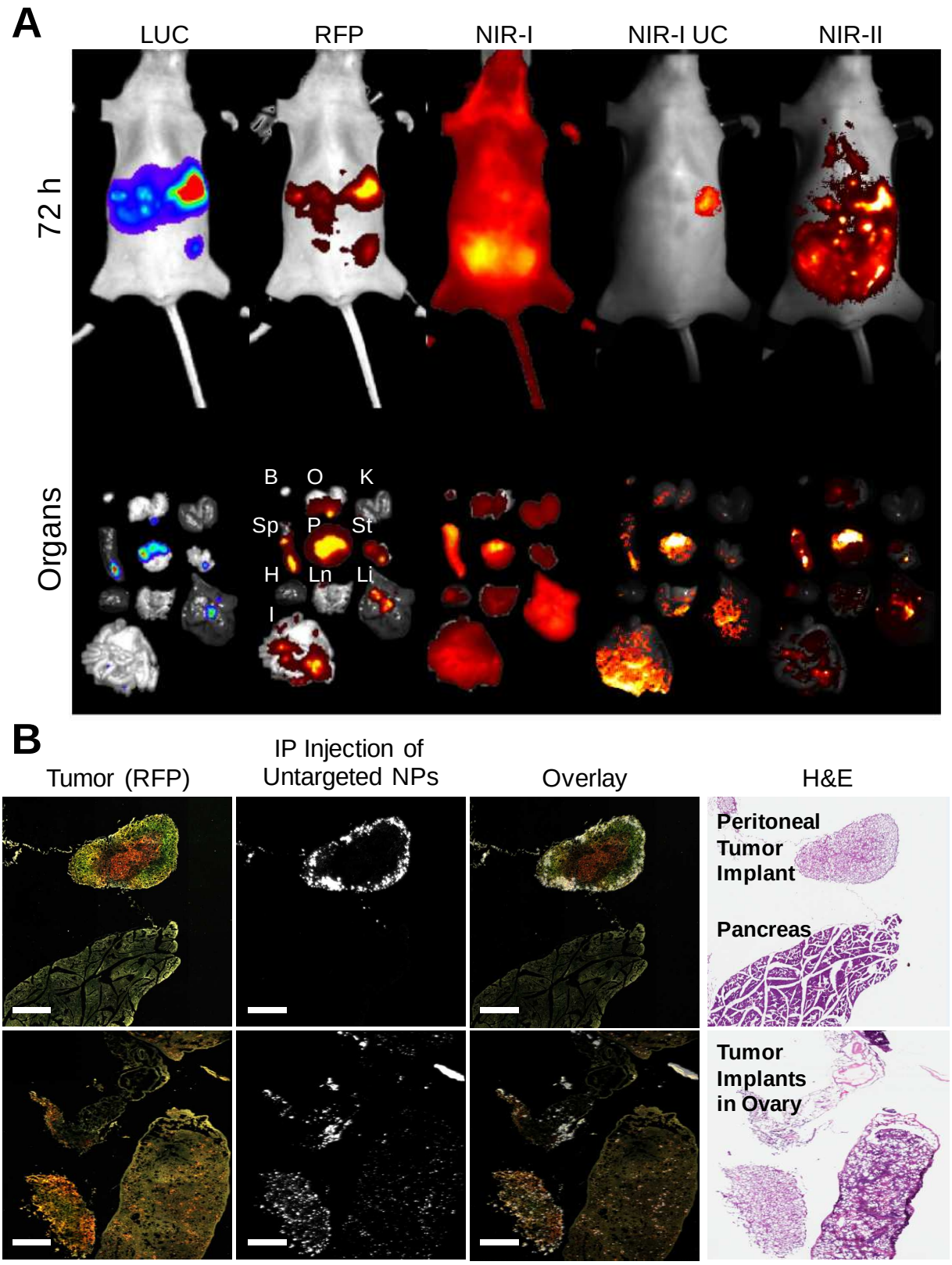

Figure 2. Tumor detection via imaging of visible, NIR-I, and NIR-II emissive signals. A) Images taken of a representative mouse at two-weeks after implantation of LUC^{+}/RFP^{+} OVCAR-8 ovarian cancer cells and 72 h after IP injection of untargeted core-shell nanoparticles (DiR-Er,Tm/PEO-PCL). *Upper Row*: *in vivo* images of intrinsic reporters (LUC and RFP) as well as various emissive components of core-shell nanoparticles (DiR and LNPs).

LUC, RPF and DiR (NIR-I) signals were detected using an IVIS imaging system; Up-conversion emission (NIR-I UC) and NIR-II fluorescence (NIR-II) emission from core LNPs were visualized using a custom designed imaging instrument (*Materials and Methods*). *Bottom Row*: *ex vivo* images were obtained after animal sacrifice and corresponded to the detection of the same reporters in excised organs, including (from left to right and from top to bottom) the bladder (B), ovaries (O), kidneys (K), spleen (Sp), pancreas (P), stomach (St), heart (H), lung (Ln), liver (Li) and intestines (I) of the animal. B) Confocal microscopy of tissue sections obtained from excised organs of the same animal. Tumors were identified by RFP fluorescence (red) while all tissues exhibited auto-fluorescence (green). Untargeted nanoparticles (NPs) were imaged by 980-nm multi-photon excitation and by detection of their visible UC emission (white). H&E staining was also performed to identify tumor implants vs. normal tissue in each organ. Scale bar = 300 μm.

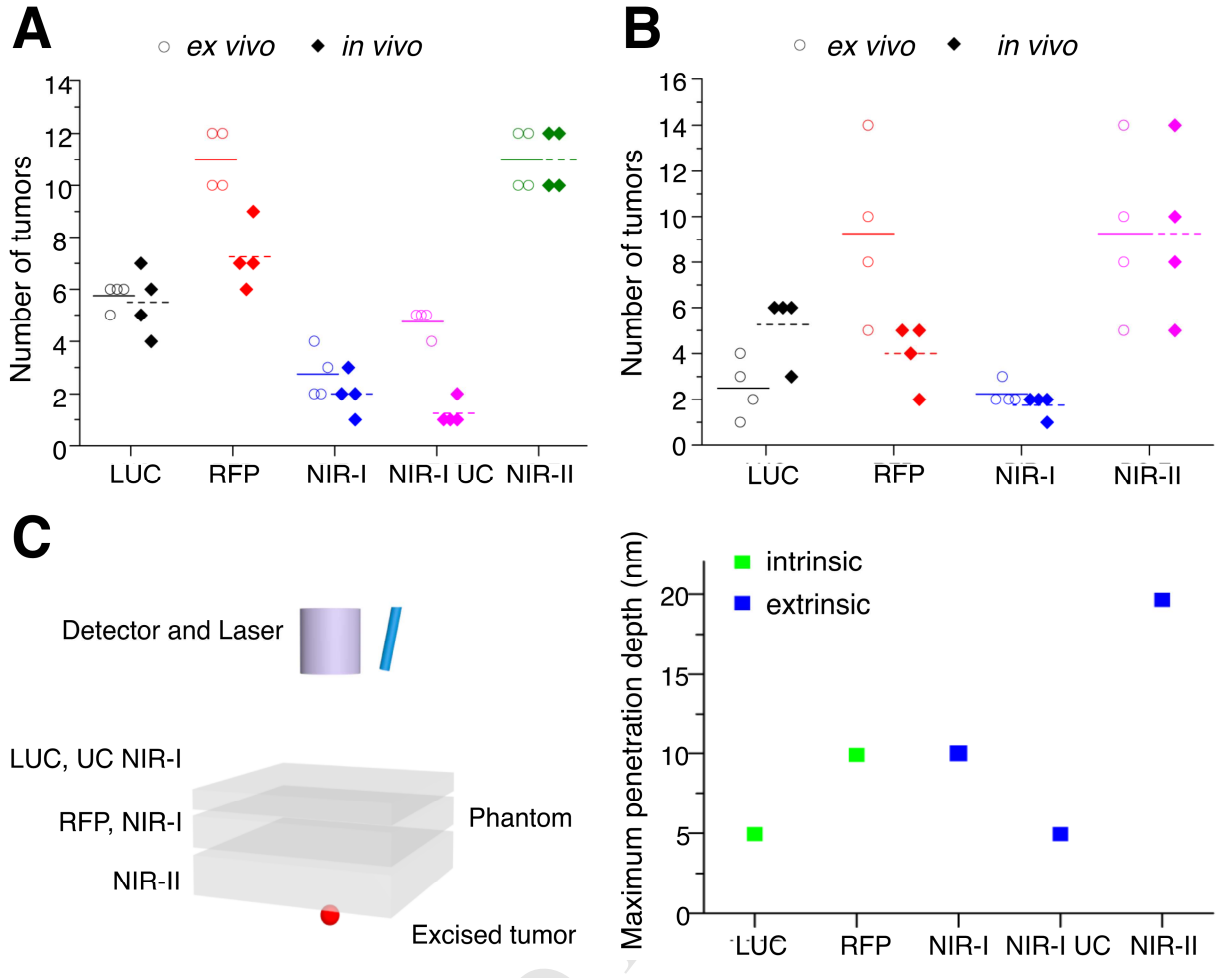

Figure 3: Comparisons of the sensitivity of various intrinsic and extrinsic reporters to detect peritoneal tumor implants. The numbers of tumors detected using different reporters were enumerated from *in vivo* vs. *ex vivo* images taken at either A) two-weeks or B) 1 week post-implantation of LUC^+/RFP^+ OVCAR-8 cells in nude mice and at 72 h after IP administration of untargeted core-shell nanoparticles (DiR-Er,Tm/PEO-PCL; n = 4 mice per group; see also Figure S9 for the numbers of tumor deposits identified from each individual mouse and via imaging of each reporter). C) Determination of the maximum depth of tissue penetration for various reporters. A tumor deposit excised from the pancreas of the mouse in Figure 2A was immersed at different depths under polymer phantoms that mimicked the optical properties of the human breast. Emissive signals emanating from the phantoms were imaged utilizing analogous techniques to those employed for *in vivo* imaging; the maximum depth of emission for a reporter was determined as the thickness of the overlying phantom at which its signal was no longer detectable. Note that DiR fluorescence (NIR-I) as well as up-conversion emission (NIR-I UC) and NIR-II fluorescence (NIR-II) from LNPs embedded in the core-shell nanoparticles (DiR-Er,Tm/PEO-PCL) were independently monitored.

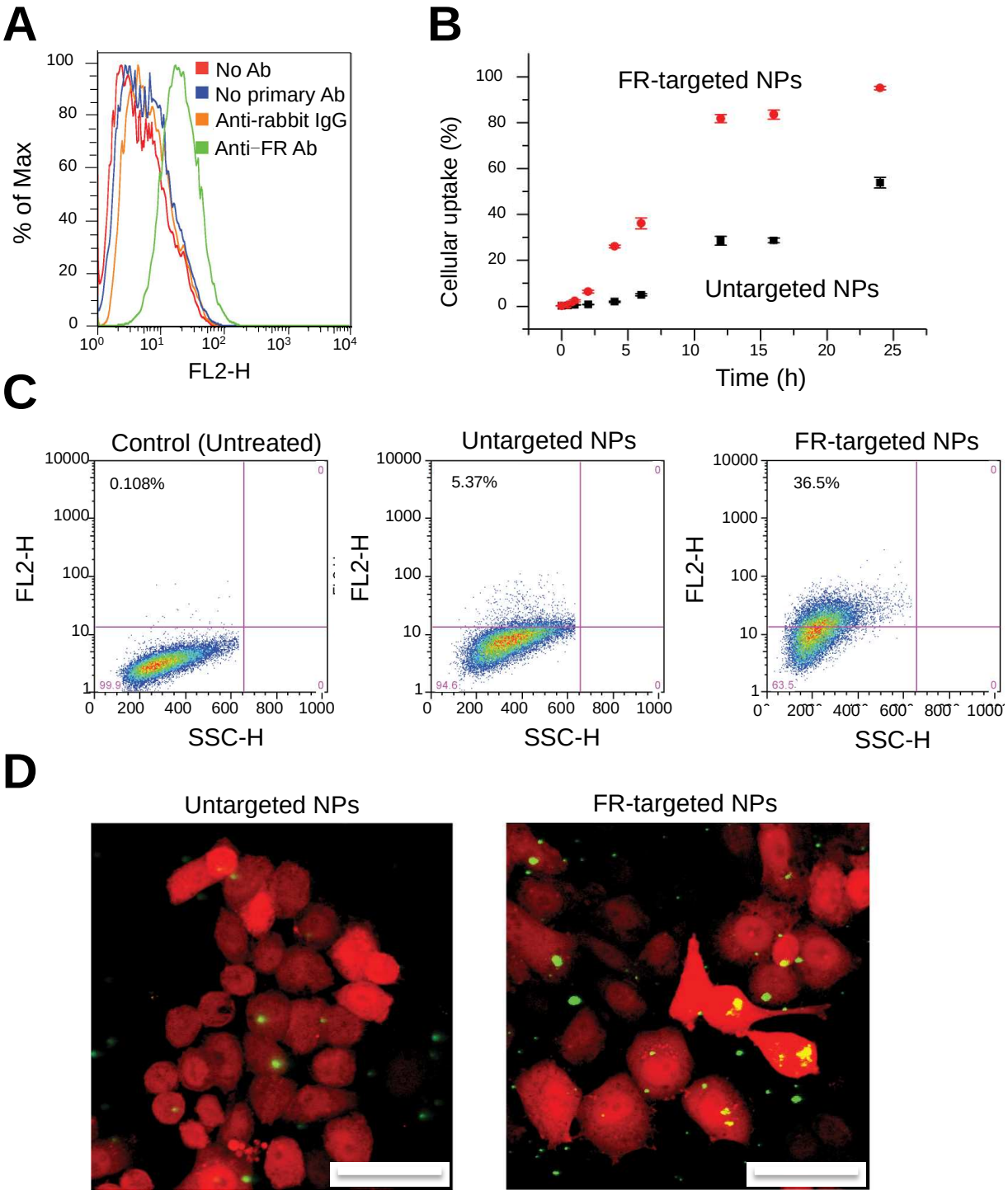

Figure 4. Examination of the role of FR-targeting to enhance *in vitro* uptake of core-shell nanoparticles by human ovarian cancer cells. A) Flow cytometry histogram demonstrating FR expression on the surface of LUC^{+}/RFP^{+} OVCAR-8 cells, using FITC-labeled mouse anti-human FR antibody (green) and several controls: no antibody (Ab) (red), no primary Ab (blue) and anti-rabbit IgG (orange). B) Relative uptake of untargeted and FR-targeted nanoparticles (NPs) as determined by flow cytometric analyses of LUC^{+}/RFP^{neg} OVCAR-8 cells over time. Untargeted (DiL/PEO-PCL) and FR-targeted NPs (DiL/Folate-PEO-PCL) were incubated with aliquots of OVCAR-8 cells for different time periods: 0, 0.5, 1, 2, 4, 6, 12, 16, and 24 h. Cells were then trypsinized, fixed, and flowed to quantify the relative levels

of DiL (λ_{em}=488 nm/λ_{ex}=585 nm) emanating from populations of intracellular nanoparticles. Note that a statistically significant increase in cellular uptake was seen for FR-targeted as compared to untargeted NPs at time points longer than 1 h (p value < 0.01). C) Representative flow cytometry histograms depicting differences in the uptake of untargeted (DiL/PEO-PCL) and FR-targeted NPs (DiL/Folate-PEO-PCL) after 6 h of incubation as compared to those of control (untreated) cells. D) Fluorescence images of LUC^+/RFP^+ OVCAR-8 cells taken after 6 h of incubation with untargeted (Er/PEO-PCL) and FR-targeted NPs (Er/Folate-PEO-PCL). Multiphoton confocal microscopy was used to image RFP (red) signals emanating from OVCAR-8 cells as well as UC emission from core LNPs (green). Scale bar = 50 μm.

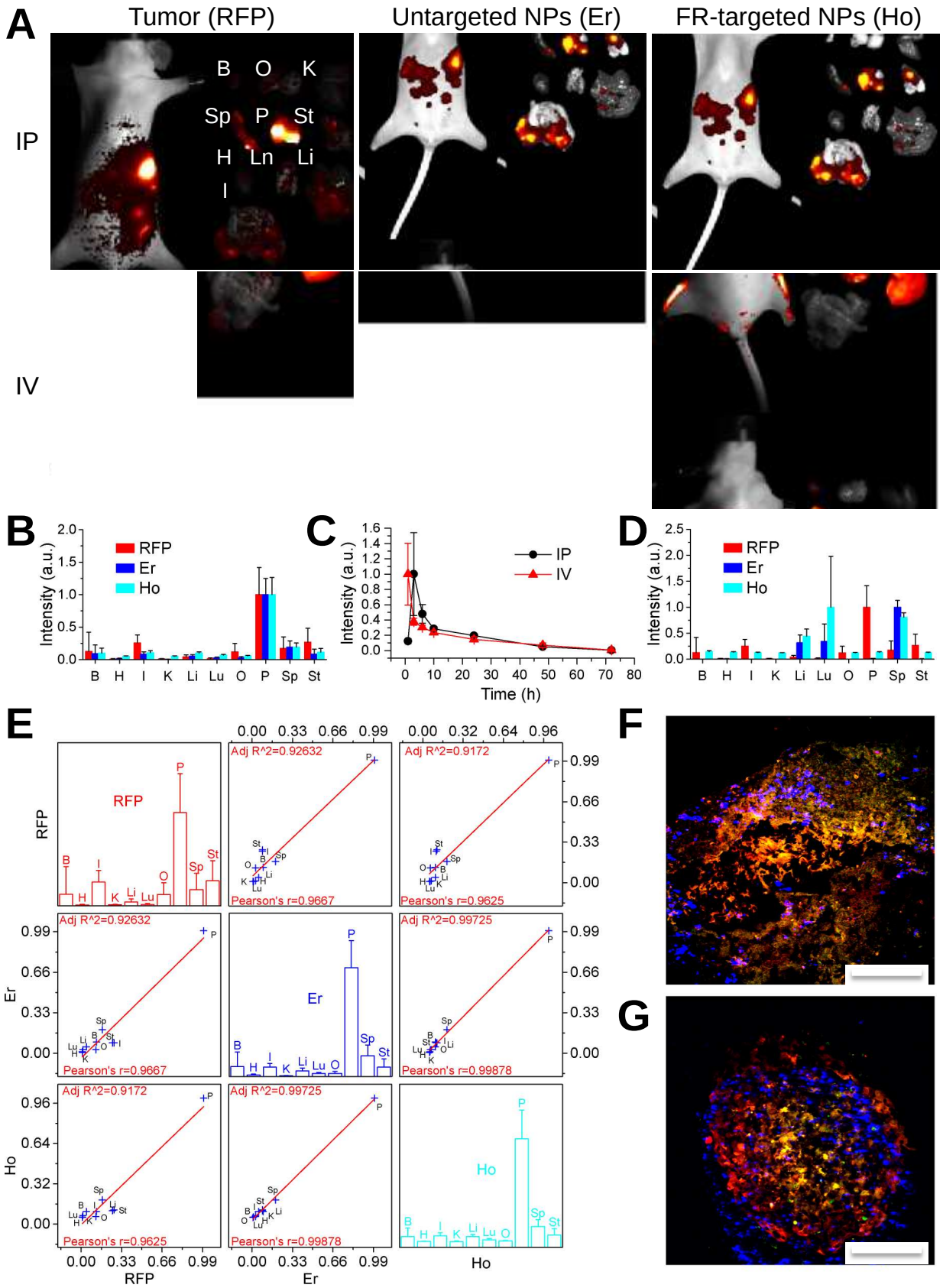

Figure 5. Determination of the optimal route of administration and the role of FR-targeting to enhance *in vivo* tumor uptake of core-shell nanoparticles. Untargeted (DiR-Er/PEO-PCL) and FR-targeted nanoparticles (DiR-Ho/Folate-PEO-PCL) were simultaneously administered to

mice via either IP or IV injection at two-weeks post-implantation of LUC^+/RFP^+ OVCAR-8 ovarian cancer cells. A) Representative images of two different mice taken at 72 h after simultaneous administration of both nanoparticles via either IP (*upper row* – mouse 1) or IV injection (*lower row* – mouse 2), detecting emission from the intrinsic reporter (RFP) as well NIR-II fluorescence from core LNPs in untargeted (Er) and FR-targeted (Ho) nanoparticles (NPs). Fluorescence intensities for each reporter were also measured in all excised organs immediately after *in vivo* imaging, including (from left to right and top to bottom) the bladder (B), heart (H), intensities (I), kidneys (K), liver (Li), lungs (Lu), ovaries (O), pancreas (P), spleen (Sp) and stomach (St) of 4 separate mice for each route of administration. B) Relative distribution of emissive signals obtained via *ex vivo* imaging of intrinsic (RFP) and extrinsic reporters (Er and Ho) in major organs at 72 h post IP-administration. For each reporter, the fluorescence intensities from all organs were normalized to the value obtained from the organ with the highest fluorescence intensity (pancreas) and are reported as the mean + SD (n = 4 mice). C) Pharmacokinetic analyses of core-shell nanoparticles in blood after IP vs. IV administration to tumor-bearing mice. D) Relative distribution of emissive signals obtained via *ex vivo* imaging of intrinsic (RFP) and extrinsic reporters (Er and Ho) in major organs at 72 h after IV administration of core-shell nanoparticles to tumor-bearing mice (n = 4 animals). *In vivo* imaging commenced and organs were processed for *ex vivo* analysis in a fashion analogous to that described in Fig. 5B (*vide supra*). E) Correlation matrix of the relative *in vivo* distribution of RFP, Er, and Ho emissive signals as determined via *ex vivo* imaging of excised organs at 72 h after simultaneous IP administration of untargeted (Er) and FR-targeted core-shell nanoparticles (Ho) to tumor-bearing mice (n = 4 animals). Each diagonal graph shows the distribution of fluorescence signals for a given reporter and correlates to the values shown in Fig. 5B. Each off-diagonal graph depicts the correlation for a pair of fluorescent reporters with a linear-fit red line, a value for the Pearson's correlation coefficient (r), and an adjusted R^2 value. Immunostaining was performed and confocal microscopy images of F) untargeted (Er/PEO-PCL) and G) FR-targeted core-shell nanoparticles (Er/Folate-PEO-PCL) were obtained to observe their intratumoral distribution (blue) with respect to tumor cells (red) and macrophages (green). Scale bar = 300 μm.

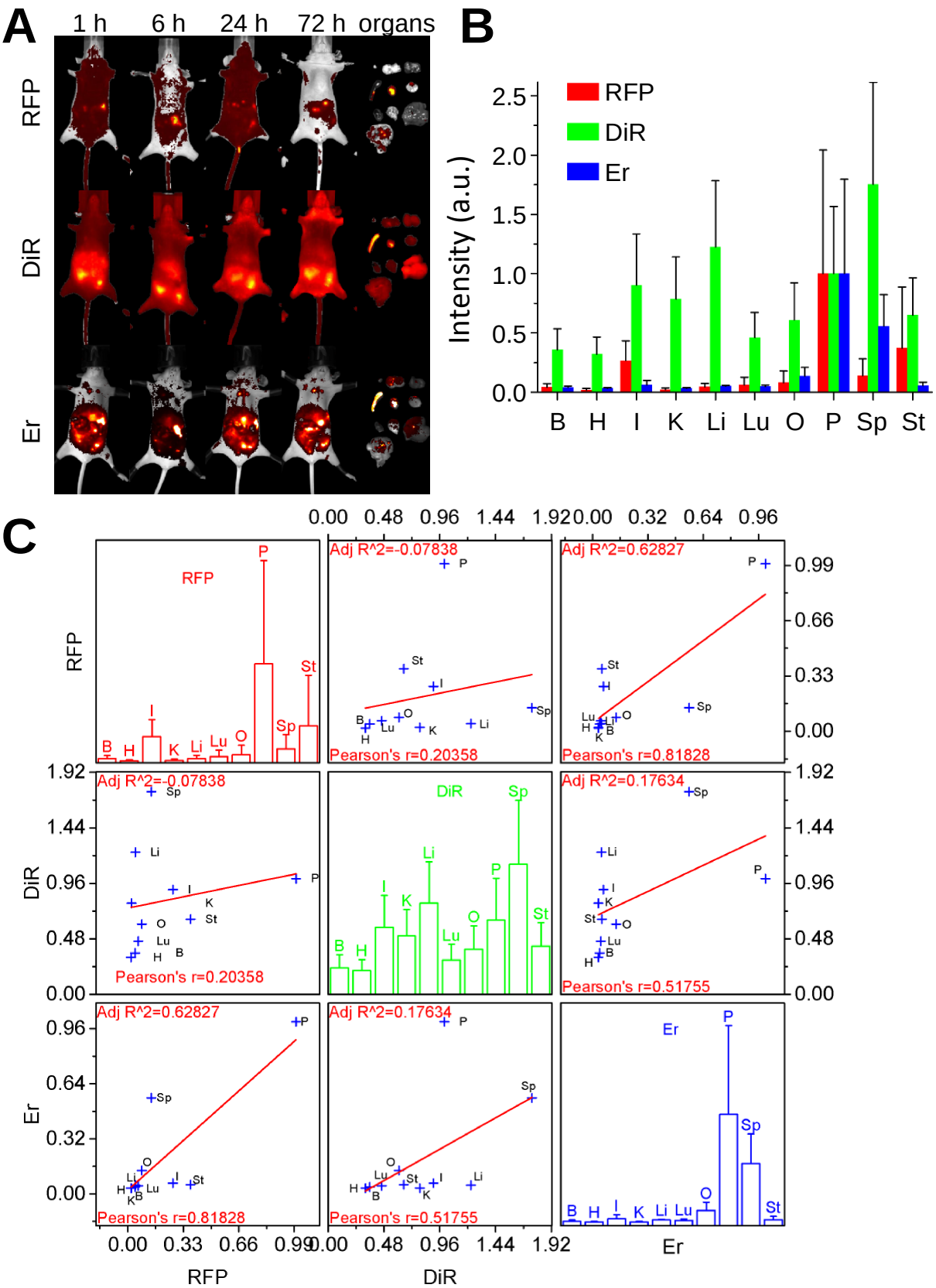

Figure 6. Early tumor detection afforded by imaging of NIR-II emission from core-shell nanoparticles. Untargeted nanoparticles (DiR-Er/PEO-PCL) were introduced into mice by IP injection at one-week post-implantation of LUC^+/RFP^+ OVCAR-8 ovarian cancer cells. A) Representative images taken at various time points after nanoparticle administration,

visualizing the distribution of NIR-I (DiR) and NIR-II emissive signals (Er) from untargeted core-shell nanoparticles in relation to the cell intrinsic reporter RFP. Fluorescence intensities for each reporter were measured in all excised organs, including (from left to right and top to bottom) the bladder (B), heart (H), intensities (I), kidneys (K), liver (Li), lungs (Lu), ovaries (O), pancreas (P), spleen (Sp) and stomach (St) of 4 separate mice that were similarly processed. B) Relative distribution of emissive signals obtained via *ex vivo* imaging of intrinsic (RFP) and extrinsic reporters (DiR and Er) in major organs at the time of animal sacrifice (72 h post administration of untargeted core-shell nanoparticles). For each reporter, the fluorescence intensities from all organs were normalized to the value obtained from the pancreas and are reported as the mean + SD (n = 4 mice). C) Correlation matrix of the relative *in vivo* distribution of RFP, DiR, and Er emissive signals as determined via *ex vivo* imaging of excised organs at 72 h after IP administration of untargeted core-shell nanoparticles to tumor-bearing mice (n = 4 animals). Each diagonal graph shows the distribution of fluorescence signals for a given reporter and correlates to the values shown in Fig. 6B. Each off-diagonal graph depicts the correlation for a pair of fluorescent reporters with a linear-fit red line, a value for the Pearson's correlation coefficient (r), and an adjusted R^2 value.